

# First results of scientific performance for the design of ESA space based gravitational wave detector (*ELISA*)

The *Science Performance Task Force*: Pau

Amaro-Seoane<sup>1</sup>, Sofiane Aoudia<sup>1</sup>, Gérard Auger<sup>2</sup>, Stanislav Babak<sup>1</sup>, Emanuele Berti<sup>3</sup> Neil J. Cornish<sup>4</sup>, Jonathan Gair<sup>5</sup>, Ryan Lang<sup>6</sup>, Tyson Littenberg<sup>6</sup>, Sean McWilliams<sup>6</sup>, Oliver Jennrich<sup>7</sup>, Philippe Jetzer<sup>8</sup>, Ioannis Kamaretsos<sup>9</sup>, Antoine Klein<sup>8</sup>, Gijs Nelemans<sup>10</sup>, Frank Ohme<sup>1</sup>, Eric Pagnol<sup>2</sup>, Antoine Petiteau<sup>1</sup>, Edward K. Porter<sup>2</sup>, Emma Robinson<sup>1</sup>, B. S. Sathyaprakash<sup>9</sup>, Bernard Schutz<sup>1</sup>, Alberto Sesana<sup>1</sup>, Carlos Sopuerta<sup>11</sup>, Alessandro Spallicci<sup>12</sup>, Ira Thorpe<sup>6</sup>, Michele Vallisneri<sup>13,14</sup>, Alberto Vecchio<sup>15</sup>, Marta Volonteri<sup>16</sup>

<sup>1</sup> Max-Planck-Institut für Gravitationsphysik (Albert-Einstein-Institut), Am Mühlenberg 1, D-14476 Golm bei Potsdam, Germany

<sup>2</sup> APC, UMR 7164, Univ. Paris 7 Denis Diderot, 10, rue Alice Domon et Leonie Duquet, 75025 Paris Cedex 13, France

<sup>3</sup> University of Mississippi, USA

<sup>4</sup> Dept. of Physics, Montana State Univ., Bozeman, MT 59717, USA

<sup>5</sup> Inst. of Astronomy, Univ. of Cambridge, Madingley Rd., Cambridge, CB30HA, UK

<sup>6</sup> Gravitational Astrophysics Lab., NASA Goddard Space Flight Center, 8800 Greenbelt Rd., Greenbelt, MD 20771, USA

<sup>7</sup> European Space Agency

<sup>8</sup> Institute of Theoretical Physics, University of Zurich

<sup>9</sup> School of Physics and Astronomy, Cardiff Univ., 5, The Parade, Cardiff, CF243YB, UK

<sup>10</sup> Department of Astrophysics, Radboud University Nijmegen, The Netherlands

<sup>11</sup> Institute of Space Sciences (ICE-CSIC), Barcelona, Spain

<sup>12</sup> University of Orleans, France

<sup>13</sup> Jet Propulsion Laboratory, California Inst. of Technology, Pasadena, CA 91109, USA

<sup>14</sup> Theoretical Astrophysics, California Inst. of Technology, Pasadena, CA 91125

<sup>15</sup> School of Physics and Astronomy, Univ. of Birmingham, Edgbaston, Birmingham B152TT, UK

<sup>16</sup> University of Michigan

E-mail: [Antoine.Petiteau@aei.mpg.de](mailto:Antoine.Petiteau@aei.mpg.de), [porter@apc.univ-paris7.fr](mailto:porter@apc.univ-paris7.fr)

## Abstract.

This document collects the current results of

<i>CONTENTS</i>	2
-----------------	---

## Contents

<b>1 Instrument configurations : noises, orbits and sensitivity</b>	<b>2</b>
1.1 Overview . . . . .	2
1.2 Noises . . . . .	2
1.2.1 Acceleration noises . . . . .	3
1.2.2 Shot noise . . . . .	4
1.2.3 Other measurement noises . . . . .	4
1.2.4 Laser noise . . . . .	4
1.3 Orbits . . . . .	4
1.3.1 LISA like orbits . . . . .	5
1.3.2 Halo around L1 . . . . .	5
1.4 Noise power spectral density (PSD) . . . . .	7
1.4.1 Analytical model . . . . .	7
1.4.2 Simulation . . . . .	7
1.5 Sensitivity . . . . .	7
1.5.1 Analytical model . . . . .	7
1.5.2 Simulation . . . . .	7
<b>2 Science return for Galactic Binaries</b>	<b>10</b>
2.1 Methodology . . . . .	10
2.2 Results . . . . .	11
2.2.1 Confusion Noise . . . . .	11
2.2.2 Recovered Source Catalogue . . . . .	11
2.2.3 Verification Binaries . . . . .	12
<b>3 Massive Black Hole binaries</b>	<b>12</b>
3.1 Parameter estimation . . . . .	12
3.1.1 PhenomC results from AEI (S. Babak, A. Petiteau, A. Sesana, F. Ohme, E. Robinson) . . . . .	12
3.2 Model selection . . . . .	13
<b>4 EMRIs</b>	<b>13</b>

### 1. Instrument configurations : noises, orbits and sensitivity

(*'section captain'* : Antoine Petiteau)

#### 1.1. Overview

During the "first phase" (before CDF), 6 configurations had been defined. The table 1 gives a summary of their main characteristics and the induced noise levels.

#### 1.2. Noises

The noise models used for the new space-based gravitational wave detector supported by ESA have been provided by ESA. Each noise includes the standard ESA margin  $M_{ESA} = 1/0.65$ .

In the following description, we give the general formulation of the root mean square value (RMS), i.e. square root of the power spectral density (PSD) in the

Configuration	C5	C4	C3	C2	C1	HL1
Armlength ( $\times 10^9$ m)	2	3	1	1	1	1 - 1.6
Orbits	analytic	analytic	analytic	$10^\circ$	closest	$20^\circ$
Diameter telescope (m)	0.28	0.25	0.25	0.4	0.4	0.25
Laser power (W)	2	0.7	0.7	2	0.05	0.7
Acceleration system	DRS	DRS	DRS	DRS	LPF <sup>(1)</sup>	DRS
Acceleration ( $10^{-48} f^{-2} \text{Hz}^{-1}$ )	6	6	6	6	$8.2 \left(1 + \frac{1.8 \times 10^4}{f^2}\right)^2$	6
Shot noise ( $10^{-38} f^2 \text{Hz}^{-1}$ )	2.05	20.07	2.31	0.06 <sup>(2)</sup>	4.92	2.31
Fixed noise ( $10^{-38} f^2 \text{Hz}^{-1}$ )	2.81	2.81	2.81	2.81	2.81	2.81

Table 1: Summary of configuration. Noises are given in  $\delta\nu/\nu$  unit.

Notes about particular cases including mistakes : (1) the margin has been taken into account 2 times ; (2) the laser power has been considered in the rms shot noise with power -1 instead of -0.5 .

standard unit of the noise. We also give the value used for each configurations in relative frequency unit  $\frac{\delta\nu}{\nu}$ .

The conversion between rms noise,  $\delta x$ , and power spectral density  $S$  is :  $S = \delta x^2$ .

The conversion between acceleration noise unit (in  $\text{m}^2 \cdot \text{s}^{-4} \cdot \text{Hz}^{-1}$ ) and noise in length unit (in  $\text{m}^2 \cdot \text{Hz}^{-1}$ ) is :

$$S(f) = S_{\text{m}^2 \cdot \text{s}^{-4} \cdot \text{Hz}^{-1}}(f) / (2\pi f)^4 \text{ m}^2 \cdot \text{Hz}^{-1} \quad (1)$$

The conversion between noise in length unit ( $\text{m}^2 \cdot \text{Hz}^{-1}$ ) and noise in relative frequency unit (in  $\text{Hz}^{-1}$ ) is :

$$S_{\frac{\delta\nu}{\nu}}(f) = S(f) \times \left(\frac{2\pi f}{c}\right)^2 \text{ Hz}^{-1} \quad (2)$$

*1.2.1. Acceleration noises* This noise is due to the limitation of the drag-free system. We consider two types of acceleration noise :

- DRS : acceleration noise corresponding to LISA requirements :

$$\delta x_{\text{acc}}^{\text{DRS}} = M_{ESA} \times 3 \times 10^{-15} \text{ m/s}^2 / \sqrt{\text{Hz}} \quad (3)$$

- LPF : acceleration noise corresponding to LISAPathfinder :

$$\delta x_{\text{acc}}^{\text{LPF}} = M_{ESA} \times 3.5 \times 10^{-15} \left(1 + \frac{0.18 \text{ mHz}}{f}\right) \text{ m/s}^2 / \sqrt{\text{Hz}} \quad (4)$$

So, we have one best case, the DRS, and one worth case, the LPF.

Note that for the LPF noise, we include the ESA margin but, according to Stefano Vitale, the margin was already taken into account in the  $3.5 \times 10^{-15}$  value. So the LPF acceleration was over-estimated (only used for configuration C1).

The acceleration noise for the different configurations is :

- for C1 :

$$S_{\text{acc}, \frac{\delta\nu}{\nu}}(f) = 8.17 \times 10^{-48} \left(\frac{1}{f} + \left(\frac{1.8 \times 10^{-4}}{f^2}\right)\right)^2 \text{ Hz}^{-1} \quad (5)$$

- for C2, C3, C4, C5, HL1 :

$$S_{\text{acc}, \frac{\delta\nu}{\nu}}(f) = 6.00 \times 10^{-48} f^{-2} \text{ Hz}^{-1} \quad (6)$$

**1.2.2. Shot noise** This noise depends directly on the received laser power after the travel between two spacecrafts. Therefore it depends on :

- $L$  : the armlength (in m),
- $D$  : the diameter of the telescope (in m),
- $P$  : the emitted laser power (in Watt)

$$\delta x_{\text{SN}} = M_{ESA} \times 7.7 \times 10^{-12} \left( \frac{1 \text{ W}}{P} \right)^{1/2} \left( \frac{L}{5 \times 10^9 \text{ m}} \right) \left( \frac{0.4 \text{ m}}{D} \right)^2 \text{ m}/\sqrt{\text{Hz}} \quad (7)$$

The acceleration noise for the different configurations is :

- for C1 :

$$S_{SN, \frac{\delta\nu}{\nu}}(f) = 4.92 \times 10^{-38} f^2 \text{ Hz}^{-1} \quad (8)$$

- for C2 :

$$S_{SN, \frac{\delta\nu}{\nu}}(f) = 6.14 \times 10^{-40} f^2 \text{ Hz}^{-1} \quad (9)$$

- for C3 :

$$S_{SN, \frac{\delta\nu}{\nu}}(f) = 2.31 \times 10^{-38} f^2 \text{ Hz}^{-1} \quad (10)$$

- for C4 :

$$S_{SN, \frac{\delta\nu}{\nu}}(f) = 2.07 \times 10^{-37} f^2 \text{ Hz}^{-1} \quad (11)$$

- for C5 :

$$S_{SN, \frac{\delta\nu}{\nu}}(f) = 2.05 \times 10^{-38} f^2 \text{ Hz}^{-1} \quad (12)$$

- for HL1 :

$$S_{SN, \frac{\delta\nu}{\nu}}(f) = 2.31 \times 10^{-38} f^2 \text{ Hz}^{-1} \quad (13)$$

**1.2.3. Other measurement noises** This noise groups to the perturbation of the optical path in the optical bench and the telescope and the precision on the interference measurement by the photodiode and the phasemeter.

$$\delta x_{\text{OMS}} = M_{ESA} \times 6.2 \times 10^{-12} \text{ m}/\sqrt{\text{Hz}} \quad (14)$$

The other measurement noise is the same for all the configurations :

- for C1,C2, C3, C4, C5, HL1 :

$$S_{OMS, \frac{\delta\nu}{\nu}}(f) = 2.81 \times 10^{-38} f^2 \text{ Hz}^{-1} \quad (15)$$

**1.2.4. Laser noise** The laser noise which have a typical rms noise around  $30 \text{ Hz} \cdot \text{Hz}^{-1/2}$  is reduced by the Time Delay Interferometry method. For this study, we suppose that the application of TDI second generation reduce the laser noise below the other noise. So it will not be consider.

### 1.3. Orbits

We use several spacecraft orbits divided in 2 types : LISA like orbits and Halo around Lagrange point L1. There are 2 key points :

- the stability of the constellation which have implication to the mission duration and on the shot noise level (see 1.2.2).
- the way of reaching the orbits which have direct budget link through the energy required

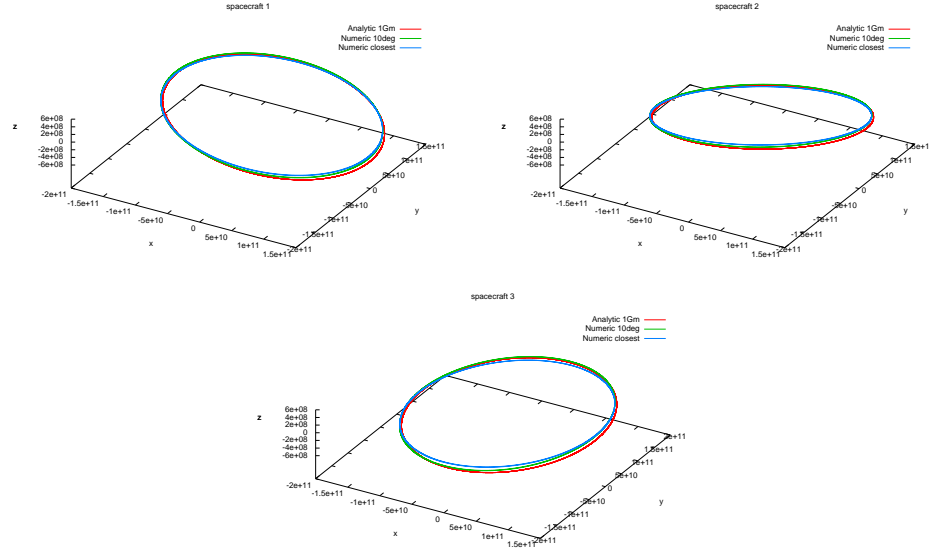


Figure 1: Orbits of the 3 spacecrafts.

**1.3.1. LISA like orbits** The LISA like orbits corresponds to constellation in a pseudo-equilateral triangle. The barycenter of the constellation follows the Earth with a certain Earth-detector barycenter angle,  $\theta_{EdB}$ . For this type of orbits, the constellation 2 key points are the armlength and the angle  $\theta_{EdB}$ . To keep the stability, if we want to increase the armlength, it implies an increase of  $\theta_{EdB}$  for limiting the tidal deformation due to the Earth.

We test 2 orbits which are the output of numerical simulation done by Oliver Jennrich (ESA) :

- best case :  $\theta_{EdB} = 10^\circ$  and  $L = 10^9$  m,
- worst case : closest to the Earth ( $\theta_{EdB} = ??^\circ$ ) and  $L = 10^9$  m,

We also use the standard analytical LISA orbits from [2] changing the armlength.

The figure 1 shows the numerical orbits compared to the analytic orbits with  $L = 10^9$  m. Regarding the position of the spacecraft the numerical orbits are close to the analytic ones. This means that the analytic orbits are a good approximation to the numeric one for computing the response of the detector to gravitational waves.

The main difference between this orbits is the time variation of the armlength as shown on the figure ???. This is an important point for the technological design of the detector (Doppler effect, ...) and for the application of the Time Delay Interferometry which is the pre-data-analysis method for reducing the laser noise.

**1.3.2. Halo around L1** We test another kind of orbits : the Halo around Lagrange point L1. This orbits are the results of numerical simulation done by Vitali Mueller (AEI-Hannover). It's a mother/daughter configuration : there are only 4 links (2 arms). The figure 3 shows the orbits and the figure 4 shows the armlength evolution.

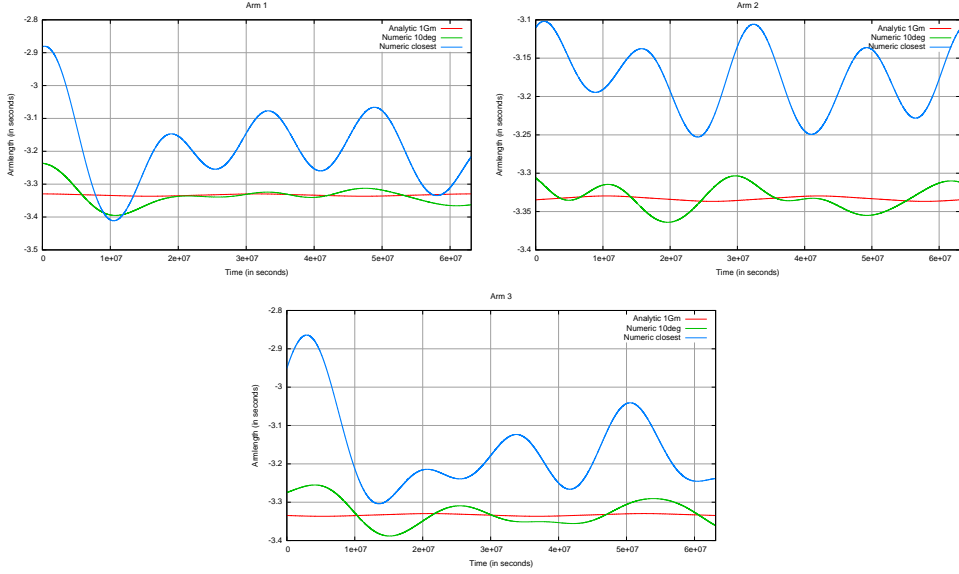


Figure 2: Time evolution of the 3 armlength during 2 years.

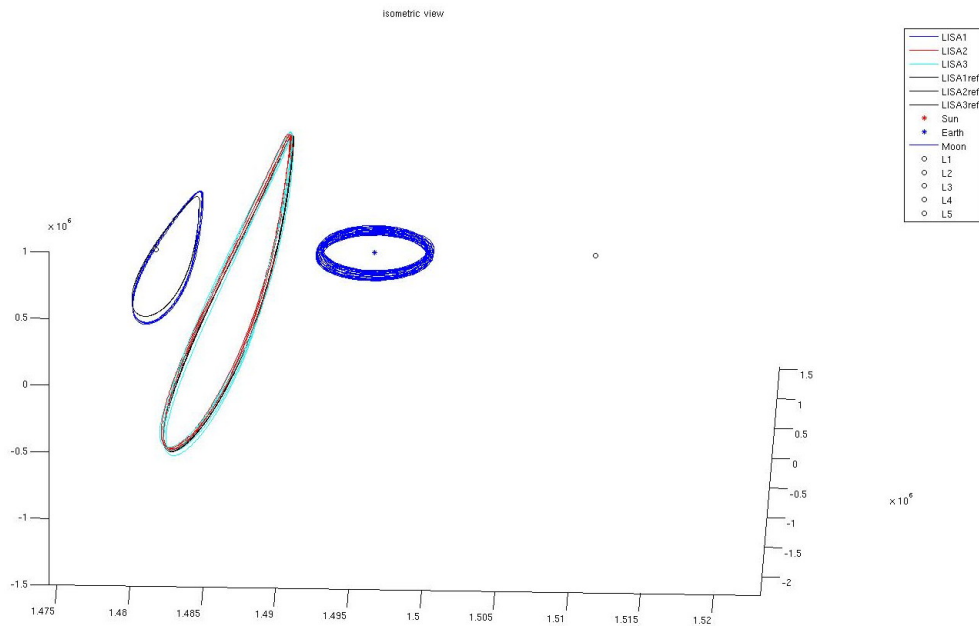


Figure 3: Orbits of spacecraft for the Halo around L1 configuration.

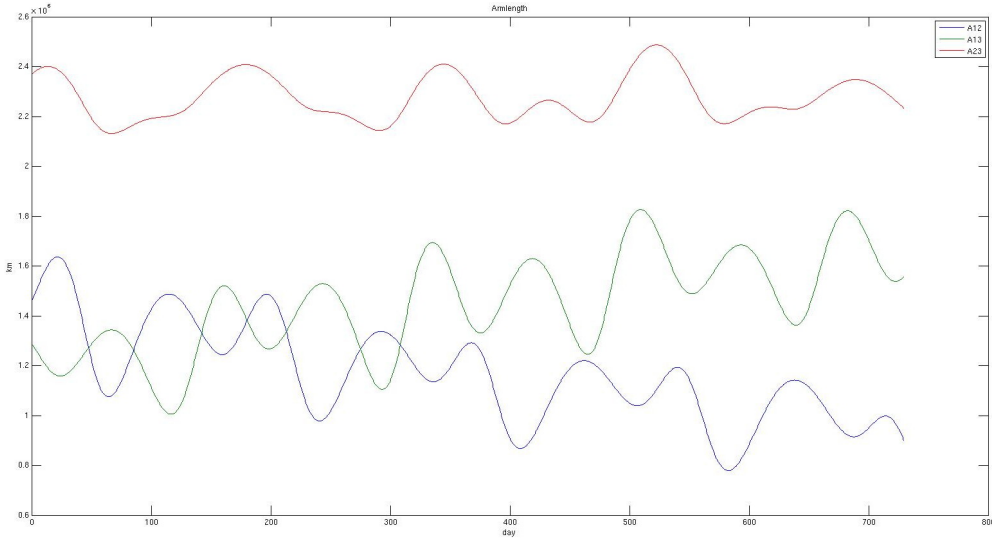


Figure 4: Evolution of armlength for the Halo around L1 configuration.

The main spacecraft (mother) is on a close orbit around L1 and the 2 daughters are on a distant orbits separated in phase by  $\pi$ . The angle between the 2 arms is around  $120^\circ$ . The armlengths evolve between 1 and 1.6 million km.

#### 1.4. Noise power spectral density (PSD)

**1.4.1. Analytical model** The analytic formulation of the Power Spectral Density of TDI X can be approximated by (usual approximation used in LISA) :

$$S_{n, \frac{\delta\nu}{\nu}}^X(f) = 16 * \sin^2(\phi_L(f)) \left( S_{SN, \frac{\delta\nu}{\nu}}(f) + S_{OMN, \frac{\delta\nu}{\nu}}(f) + (3 + \cos(2\phi_L(f))) S_{acc, \frac{\delta\nu}{\nu}}(f) \right) \quad (16)$$

with  $\phi_L(f) = 2\pi f L/c$

#### 1.4.2. Simulation

#### 1.5. Sensitivity

**1.5.1. Analytical model** (Very) approximative analytic formulation (based on LISA science requirements document (2010)) :

The transfert function is

$$T(f) = \sqrt{1 + \left( \frac{f}{(0.41 (\frac{c}{2L}))} \right)^2} \quad (17)$$

Sensitivity formulation :

$$\sqrt{S_h^X(f)} = \sqrt{5} \frac{2}{\sqrt{3}} T(f) \frac{\sqrt{4S_{acc} + S_{SN} + S_{omn}}}{L} \quad (18)$$

#### 1.5.2. Simulation

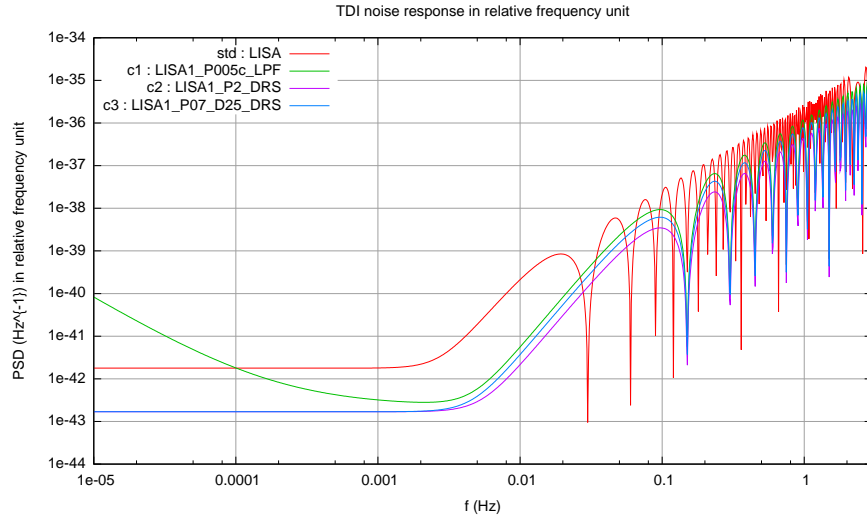


Figure 5: Comparison of power spectral density of noises' response for standard LISA, configurations 3a, 4a and 5a

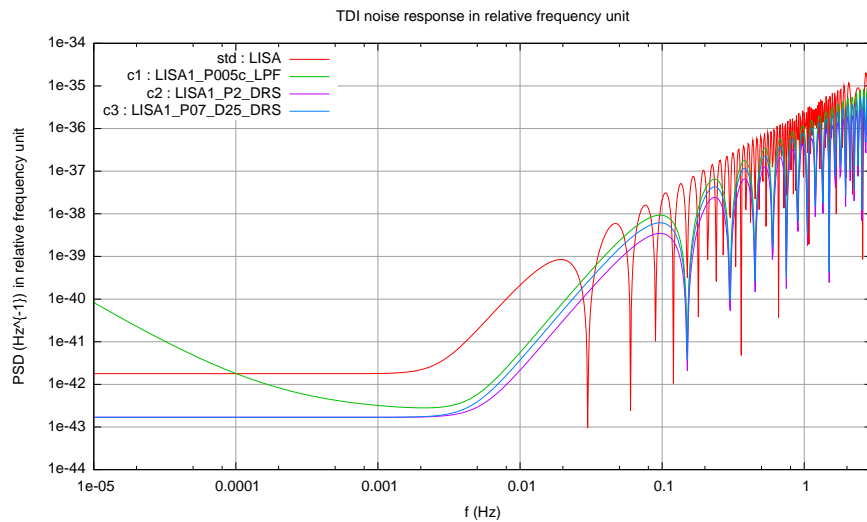


Figure 6: Comparison of power spectral density of noises' response for standard LISA, configurations 1c, 2 and 3

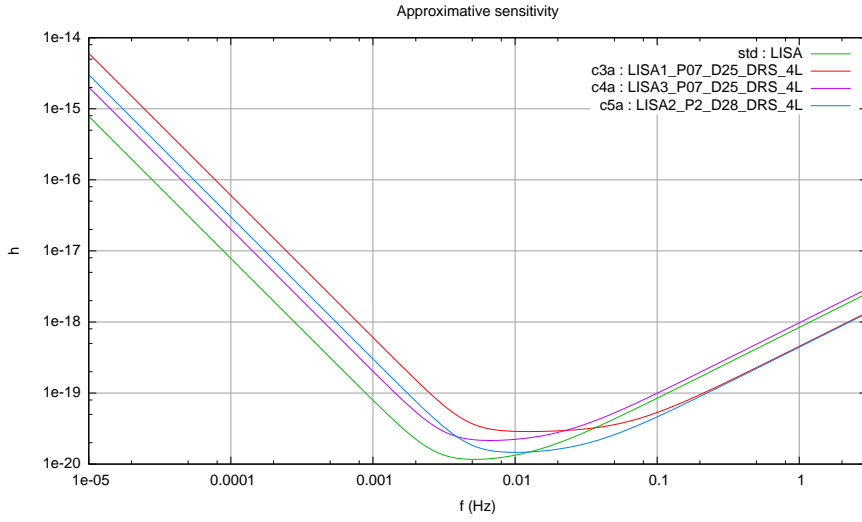


Figure 7: Comparison of sensitivity (SNR=1, "instantaneous") for standard LISA, configurations 3a, 4a and 5a

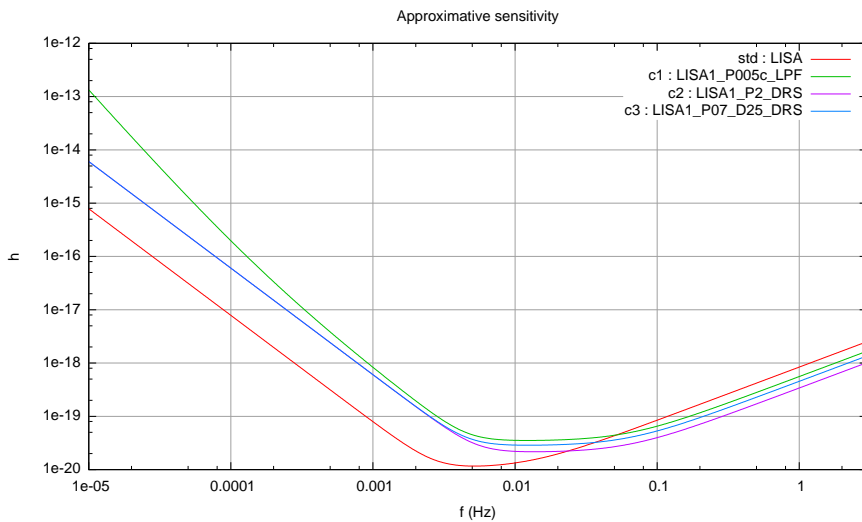


Figure 8: Comparison of sensitivity (SNR=1, "instantaneous") for standard LISA, configurations 1c, 2 and 3

## 2. Science return for Galactic Binaries

(‘section captain’ : Tyson Littenberg)

Here we summarize the detection capabilities for Galactic Binaries with different ELISA configurations.

### 2.1. Methodology

The galactic confusion estimation is performed using the `GB_confusion` package of codes which have been incorporated into `lisatools/MLDCwaveforms`. Included in the directory on the SVN repository are example files, run scripts and a (readable?) `README`.

To estimate the confusion noise we first simulate the instrument response to the galactic foreground by generating and co-adding waveforms for each source in the simulated galaxy downloaded from

<https://lisa-light.aei.mpg.de/bin/view/GalacticBinaries/PopulationGalacticBinaries>

The `GB_confusion` codes expect the source catalogue to be in the “MLDC” file format, i.e. with columns

$$f_0, \dot{f}_0, \theta, \phi, A_0, \iota, \psi, \varphi_0.$$

Parameters  $f$  is the GW frequency, subscript 0 denotes values measured at the start of the mission observation,  $\{\theta, \phi\}$  are the ecliptic latitude and longitude of the source in radians,  $A$  is the amplitude, and  $\{\iota, \psi, \varphi_0\}$  are the inclination, polarization, and initial wave phase, together describing the orientation of the binary with respect to the line of sight from the solar system barycenter (SSB). The `PopulationGalacticBinaries` sources are parameterized by their orbital period (and  $\dot{P}$ ), the component masses of the binary, the luminosity distance, and the sky-location in galactic coordinates, so the appropriate conversions need to be applied *a priori*. Also, the supplied galaxy simulations are over-populated with interacting binaries (those with  $\dot{f}_0 < 0$  by a factor of  $\sim 10$ ). We account for this by randomly culling 90% of mass-transferring binaries from the population before computing the instrument response. While the TDI signals from the galaxy are being simulated, any binaries with signal-to-noise ratio (SNR) greater than one are stored in a separate “Brights” file which will later be analyzed to determine which are detectable.

With the simulated data in hand, we iteratively estimate the confusion noise by dividing the Fourier domain data into  $\sim 30$  segments between  $\sim 10^{-4}$  and  $\sim 10^{-1}$  Hz and compute the median Fourier power in each segment. The SNR for each signal in the Brights file is computed against this confusion noise (plus instrument noise), and any with signal-to-noise greater than 7 are stored as “detectable” and removed from the data. This process is repeated iteratively until the confusion estimation converges. The analysis is performed simultaneously considering 4- and 6-link configurations, producing separate results for the Michelson “X” channel (4 links) and noise orthogonal “AET” channels (6 links).

To understand the parameter estimation capabilities of different configurations, the lower-bound on the uncertainties for each source’s parameters are computed using the Fisher Information Matrix (FIM), using the instrument + confusion noise as the weighting in the inner products. We separately report on the number of signals w/  $\dot{f}$  measured w/in 20% as a proxy for number with measurable  $D_L$ . Using only  $\dot{f}$  to disentangle the distance from the overall amplitude implicitly assumes that the

binary's dynamics are dominated by the radiation reaction force. To unequivocally verify this assumption, we also need to measure the second time derivative of the frequency which was a difficult task even for LISA.

## 2.2. Results

### 2.2.1. Confusion Noise

The confusion noise estimates for each configuration under consideration are shown in Figure 9. The green [dashed] traces show the instrument noise. The red [solid] curves are the full noise spectra with confusion noise included, illustrating the impact of the astrophysical foreground on the instrument sensitivity. The black [dotted] lines are the LISA baseline instrument noise, and are included for reference. All estimates are for two year observation times. The confusion noise does not have a significant impact on the detector sensitivity for the 1 Gm configurations.

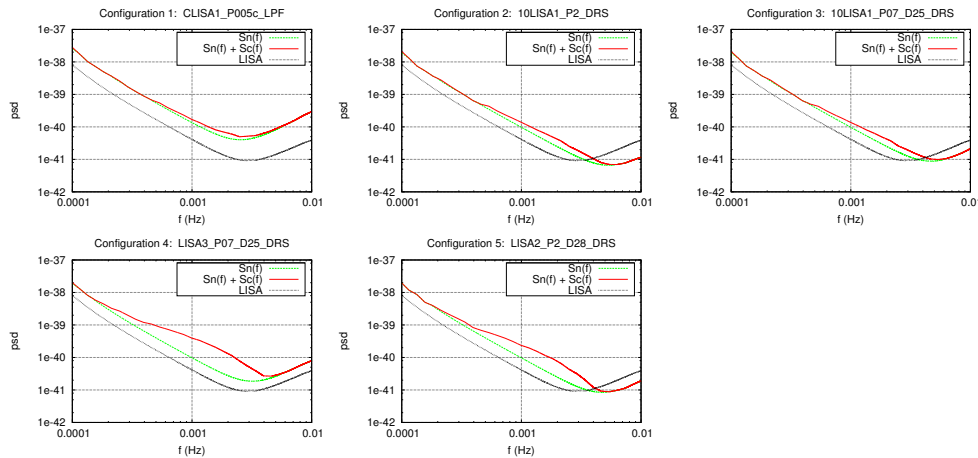


Figure 9: Noise spectra for different detector configurations. The red [solid] curves show the full noise spectrum, the green [dashed] curves are the instrument-only noise spectra and the black [dotted] line is the baseline LISA instrument noise curve. All results are for two year mission lifetimes.

### 2.2.2. Recovered Source Catalogue

Here we use the lists of detectable binaries and the FIM to make very coarse statements about the science potential for the different configurations. Table 2 summarizes the parameter estimation results. Of the total number of detectable binaries (shown in the  $\text{SNR} > 7$  column of the table), the number of which that can be resolved on the sky to  $\approx 1 \text{ deg}^2$  are separately tabulated. This number ranges between a few hundred to  $\sim 2000$  for the most sensitive configuration. Binaries with a fractional error in  $\dot{f}_0$  of less than 20% are of particular interest, as the frequency evolution can be used to constrain the luminosity distance to the source. Perhaps the most astrophysically interesting number is in the final column of Table 2, which shows the number of detectable binaries that are both well localized in the sky and have potentially well constrained luminosity distances. It is from this sub-population of detectable binaries that the 3D spatial distribution of the Galaxy can

be directly probed. The bottom row of the table shows the results for the baseline LISA design.

The evaluation software also tracks the number of binaries with  $\ddot{f}_0$  constrained to within 20%. This quantity is required to unambiguously determine if the orbital period of the binary is being solely driven by the emission of gravitational waves, or if there is some additional dynamical interaction between two stars. Unfortunately, for the new configurations being considered, only a few binaries will have sufficiently well constrained  $\ddot{f}$  during a two year observation time. This is not all that surprising, as the prospects for measuring  $\ddot{f}_0$  with LISA were uncertain at best.

	Detector Configurations	$\text{SNR} > 7$ 4-link (6-link)	$\Delta\Omega \approx 1 \text{ deg}^2$ 4-link (6-link)	$\Delta\dot{f}/\dot{f} \leq 20\%$ 4-link (6-link)	$\{\theta, \phi, D_L\}$ 4-link (6-link)
1:	CLISA1_P005c_LPF	1071 (1846)	149 (387)	290 (469)	33 (55)
2:	10LISA1_P2_DRS	4586 (6204)	1107 (1892)	1331 (1678)	370 (457)
3:	10LISA1_P07_D25_DRS	4087 (5735)	932 (1679)	1176 (1510)	286 (357)
4:	LISA3_P07_D25_DR	7058 (12754)	1527 (2997)	1563 (2093)	465 (616)
5:	LISA2_P2_D28_DRS	6827 (11272)	1821 (3150)	1814 (2284)	628 (814)

Table 2: Summary of FIM parameter estimation results for the ensemble of detectable binaries for each configuration, considering both 6-link and 4-link operations. All results are for two year mission lifetimes.

### 2.2.3. Verification Binaries

## 3. Massive Black Hole binaries

### 3.1. Parameter estimation

(‘section captains’: Neil Cornish & Emanuele Berti)

**3.1.1. PhenomC results from AEI (S. Babak, A. Petiteau, A. Sesana, F. Ohme, E. Robinson)** We use PhenomC waveforms described in [1]. Waveforms include merger and ringdown and assume aligned spins. Given the latter assumption, we apply them to efficient accretion models (SE, LE) only. Moreover, since the waveforms can not handle too extreme cases, we lower the maximal spin limit to 0.98, and considered only sources with mass ratio larger than  $q = M_2/M_1 = 0.05$ , thus loosing 10-20% of the sources (depending on the MBH population model) in our analysis.

We consider a threshold  $\text{SNR} = 6$  for detection, and  $\text{SNR} = 10$  for trustworthy parameter estimations. We show results for detectors LISA, C4, C5, C2, C3 and C5, assuming a single Michelson interferometer.

Figures 10 and 11 show histograms of parameter estimation accuracy for the ten realizations of model SE and LE respectively with LISA, C2, C4 and C5; only sources with  $\text{SNR} > 10$  are included.

The median parameter estimation accuracy with LISA, C2, C4 and C5 as a function of redshift is shown in figures 14-to-15.

The median source SNR with LISA, C2, C4 and C5 as a function of redshift is shown in figures 14-to-15.

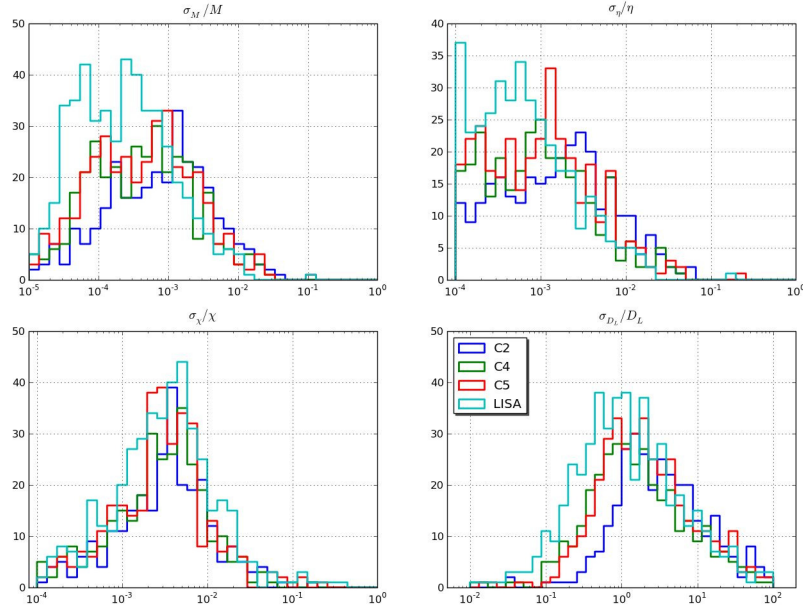


Figure 10: 1- $\sigma$  errors on source parameters: redshifted mass (upper left); symmetric mass ratio (upper right); spin parameter (lower left); luminosity distance (lower right). Histograms collect all the events in the SE catalogue (small seed), with SNR > 10. Light blue histograms are for LISA, blue histograms are for C2, green histograms are for C4 and red histograms are for C5.

For comparison we also add results comparing about C1, C2 and LISA and SNR for C3 :

Figures 16, 17, 18 and 19 show the performances of LISA, C2 and C1 respectively, assuming the SE MBH binary population model.

Figures 20 and 21 show histograms of parameter estimation accuracy for the ten realizations of model SE and LE respectively; only sources with SNR > 10 are included.

The median source SNR and parameter estimation accuracy as a function of redshift is shown in figures 23-to-25.

### 3.2. Model selection

('section captain' : Alberto Sesana)

## 4. EMRIs

('section captains' : Jon Cair & Ed Porter)

- [1] L. Santamaría, F. Ohme, P. Ajith, B. Bruegmann, N. Dorband, M. Hannam, S. Husa, P. Moesta, D. Pollney, C. Reisswig, E. L. Robinson, J. Seiler and B. Krishnan, Phys. Rev. D **82**, 064016 (2010)

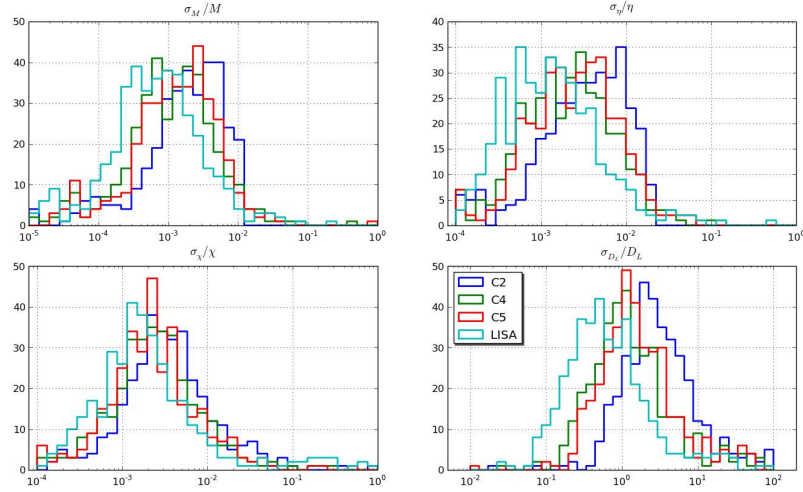


Figure 11:  $1-\sigma$  errors on source parameters. Similar as 10 with LE catalogue (large seed).

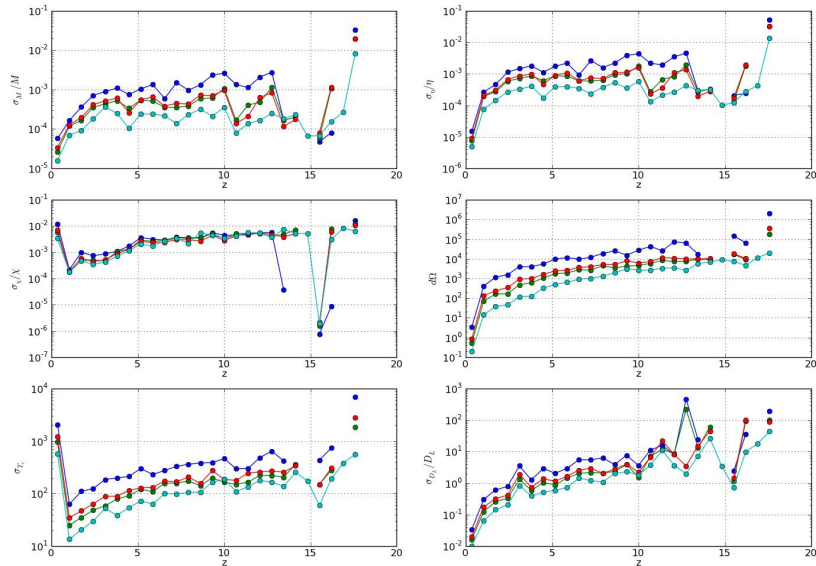


Figure 12: Median  $1-\sigma$  errors on the source parameters as a function of  $z$ : redshifted mass (upper left); symmetric mass ratio (upper right); spin parameter (middle left); sky location in  $\text{deg}^2$  (middle right); coalescence time in seconds (lower left); luminosity distance (lower right). Colorstyle as in figure 10 : light blue histograms are for LISA, blue histograms are for C2, green histograms are for C4 and red histograms are for C5. Model SE (small seeds) is assumed.

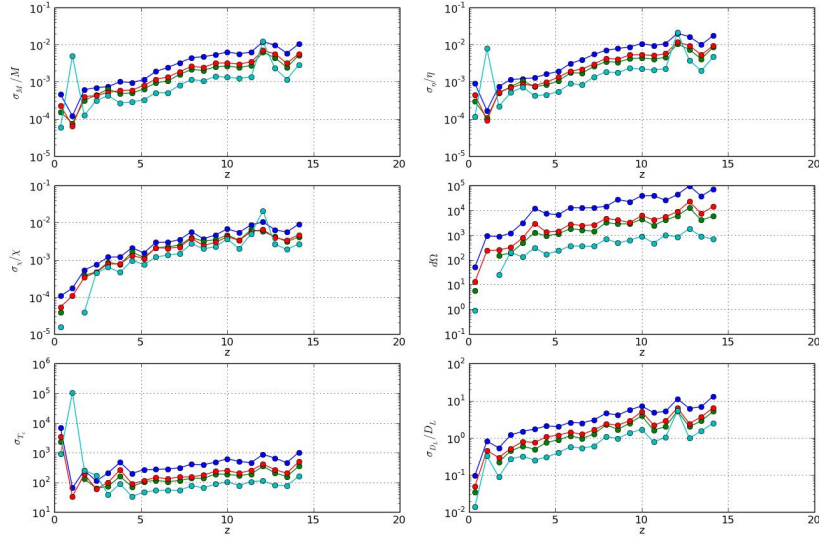


Figure 13: Same as figure 12 but for the LE (large seed) catalogue.

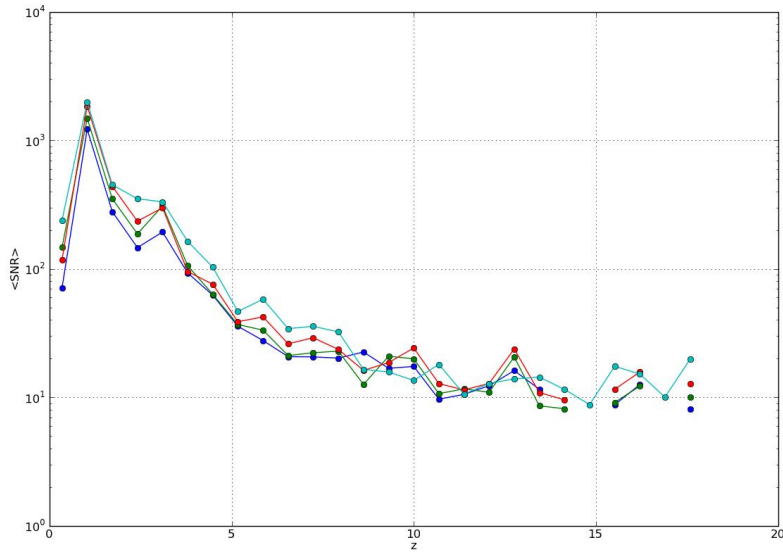


Figure 14: Median SNR  $s$  as a function of  $z$ . Colorstyle as in figure 10 : ligh blue histograms are for LISA, blue histograms are for C2, green histograms are for C4 and red histograms are for C5. Model SE (small seeds) is assumed.

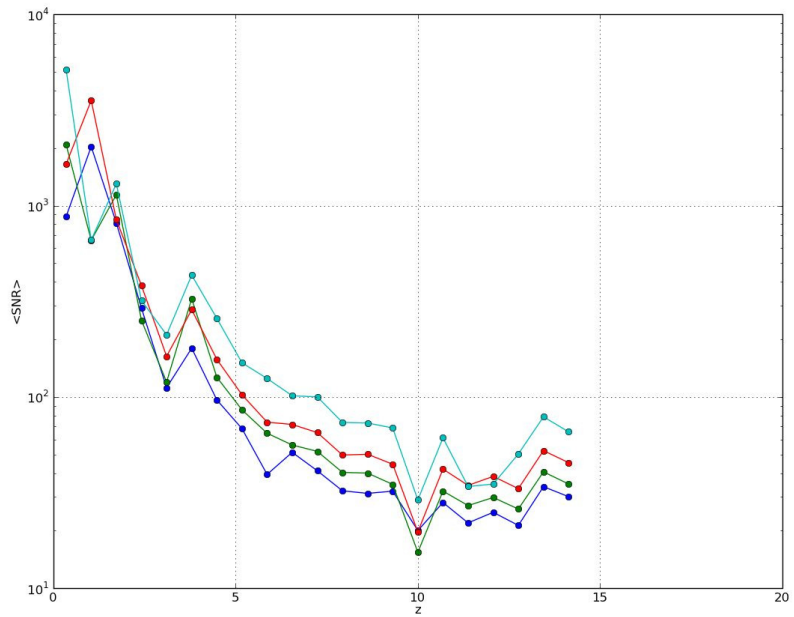


Figure 15: Same as figure 14 but for the LE (large seed) catalogue.

- [2] Dhurandhar, S. V. and Nayak, K. R. and Koshti, S. and Vinet, J.-Y. Classical and Quantum Gravity **22**, 481-487 (2005)

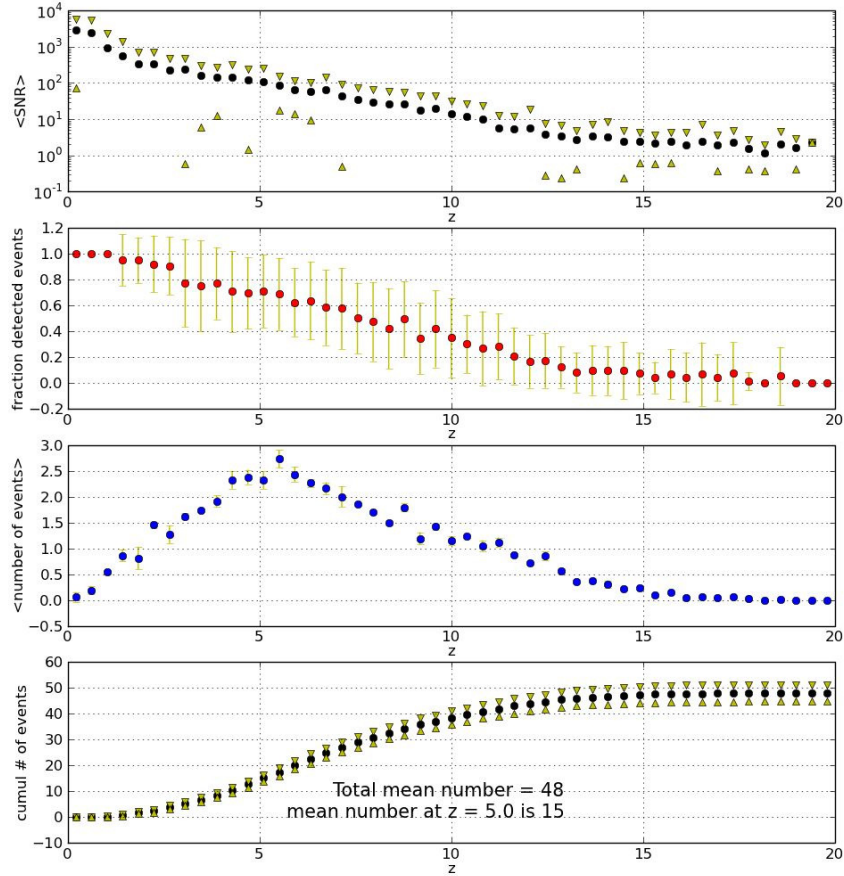


Figure 16: LISA performances as a function of redshift. From the top to the bottom we plot the average source SNR, the fraction of detectable sources ( $\text{SNR} > 6$ ), the mean number of detected sources, and the cumulative number of detected sources. Error bars are standard deviations; SE population model is assumed.

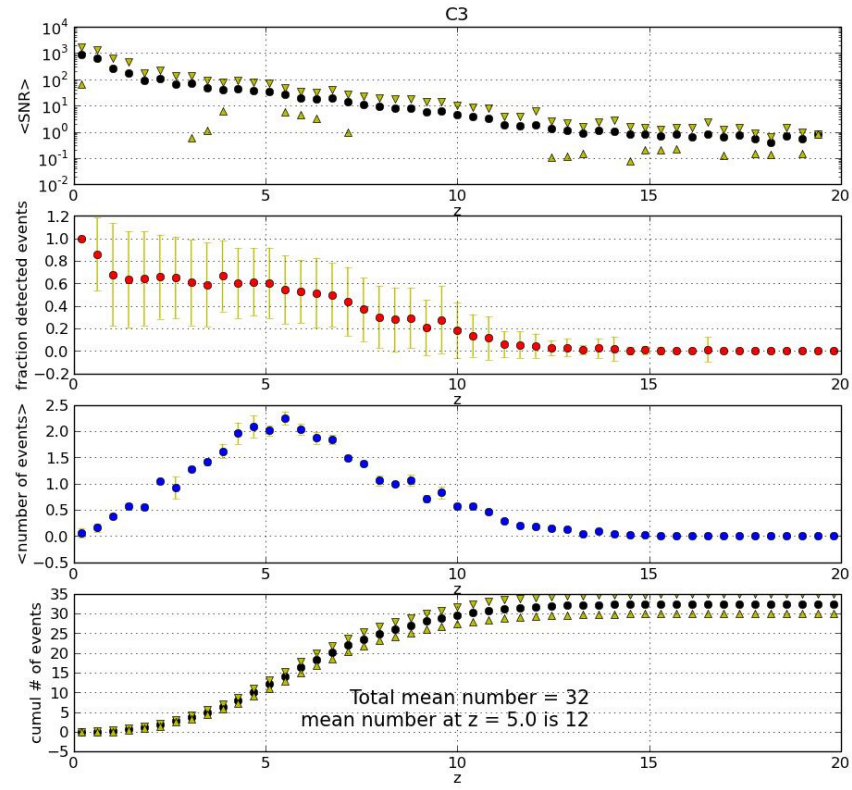


Figure 17: Same as figure 16 but for C3.

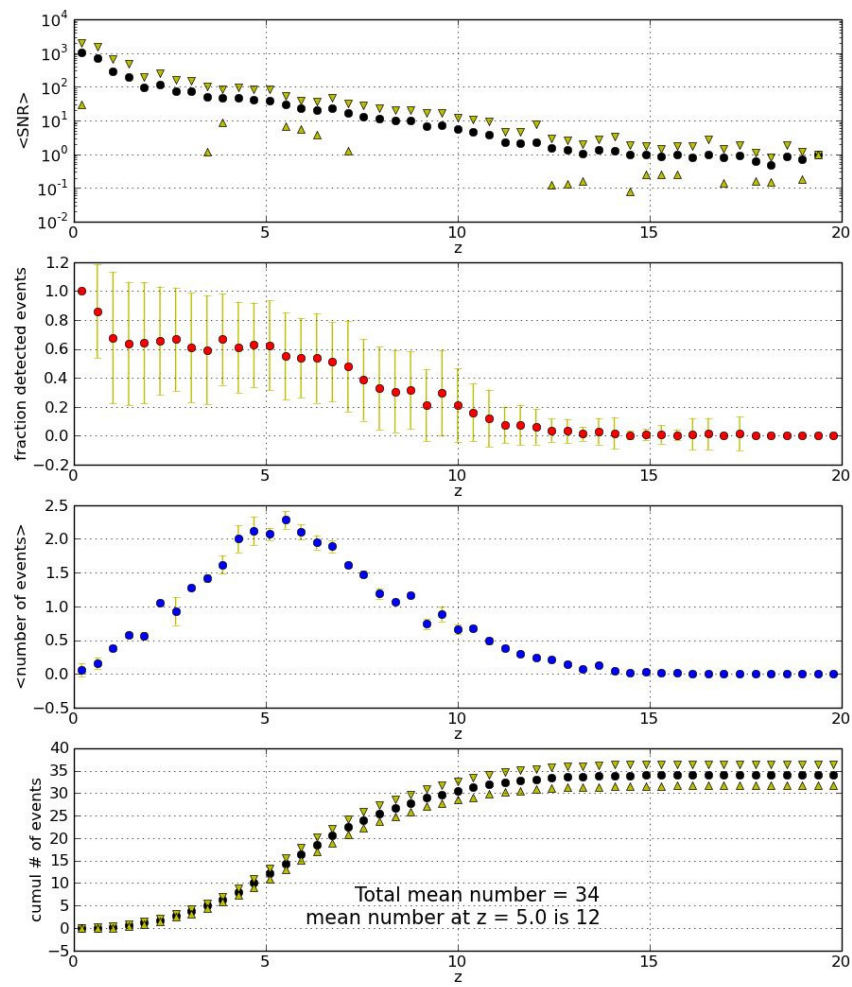


Figure 18: Same as figure 16 but for C2.

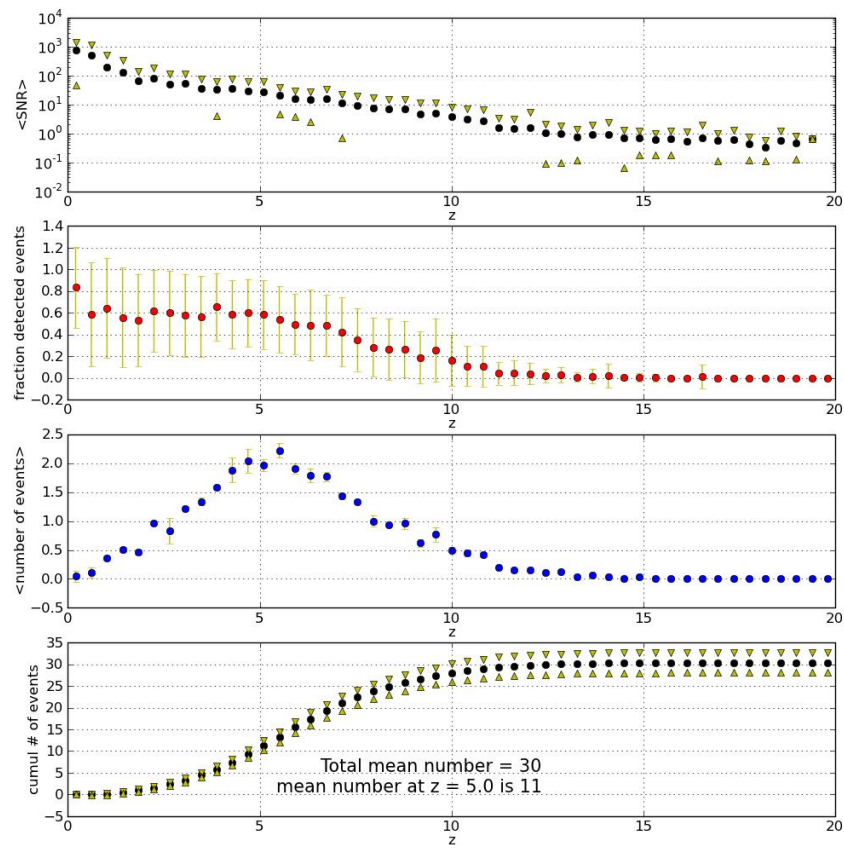


Figure 19: Same as figure 16 but for C1.

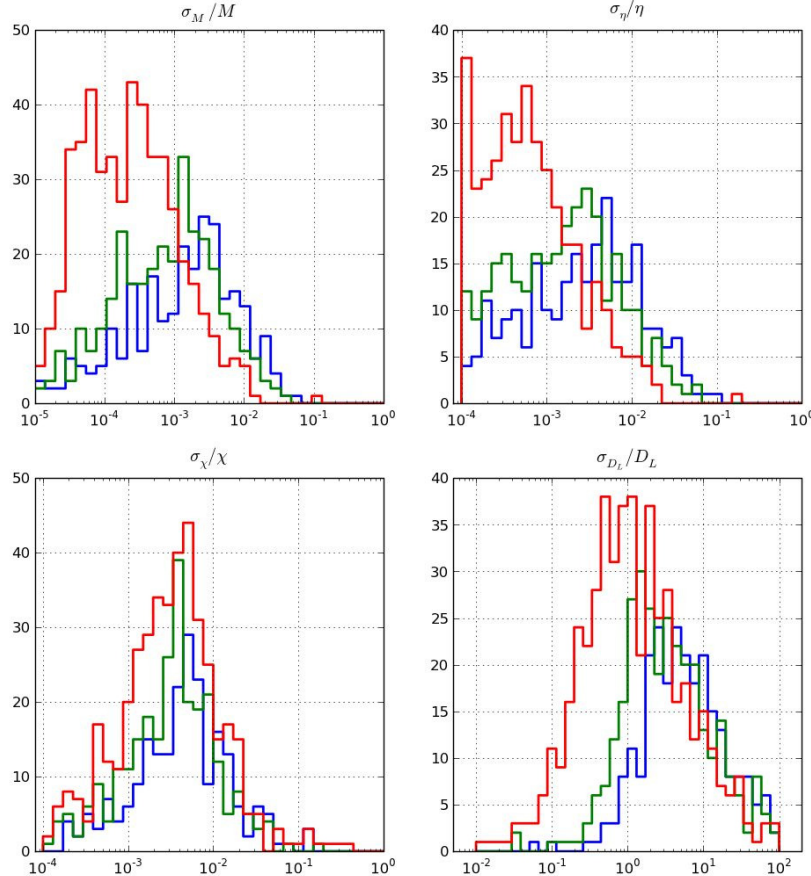


Figure 20:  $1-\sigma$  errors on source parameters: redshifted mass (upper left); symmetric mass ratio (upper right); spin parameter (lower left); luminosity distance (lower right). Histograms collect all the events in the SE catalogue, with  $\text{SNR} > 10$ . Red histograms are for LISA, green histograms are for C2 and blue histograms are for C1.

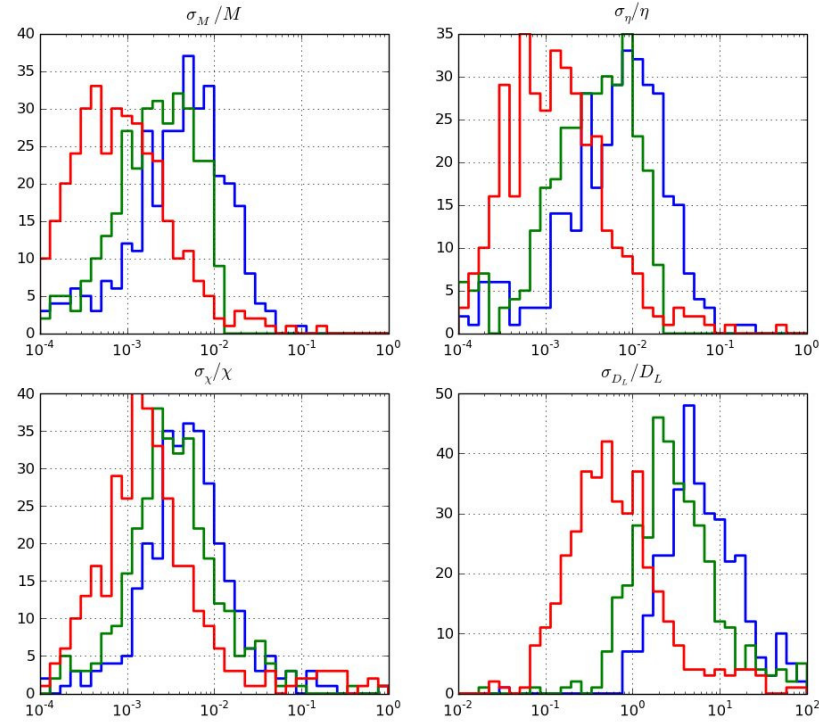


Figure 21: Same as figure 20 but for the LE catalogue.

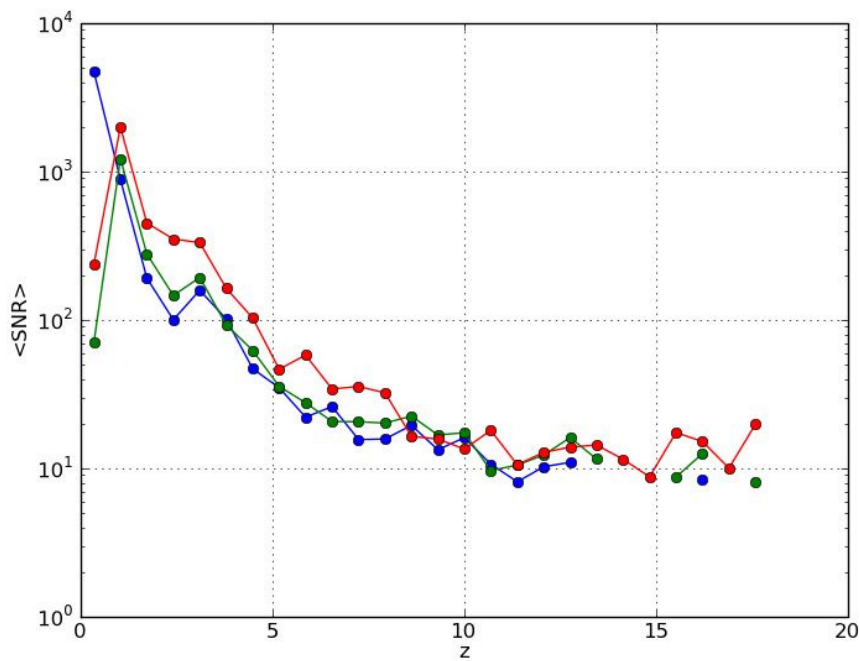


Figure 22: Median source SNR as a function of  $z$ . Colorstyle as in figure 20. Model SE is assumed.

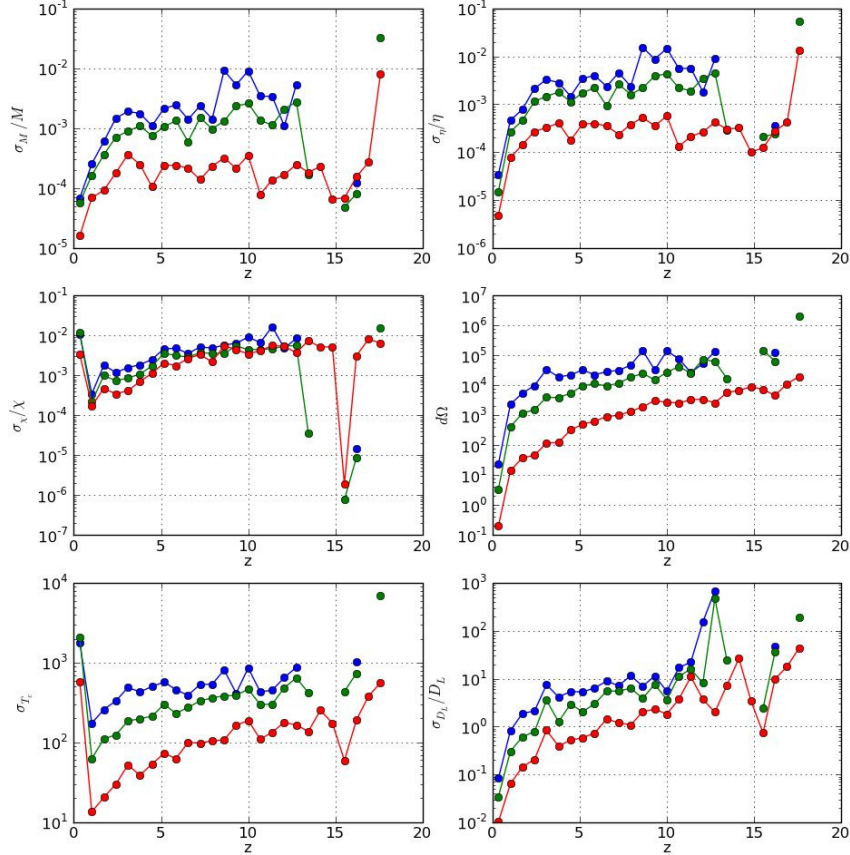


Figure 23: Median 1- $\sigma$  errors on the source parameters as a function of  $z$ : redshifted mass (upper left); symmetric mass ratio (upper right); spin parameter (middle left); sky location in deg<sup>2</sup> (middle right); coalescence time in seconds (lower left); luminosity distance (lower right). Colorstyle as in figure ???. Model SE is assumed.

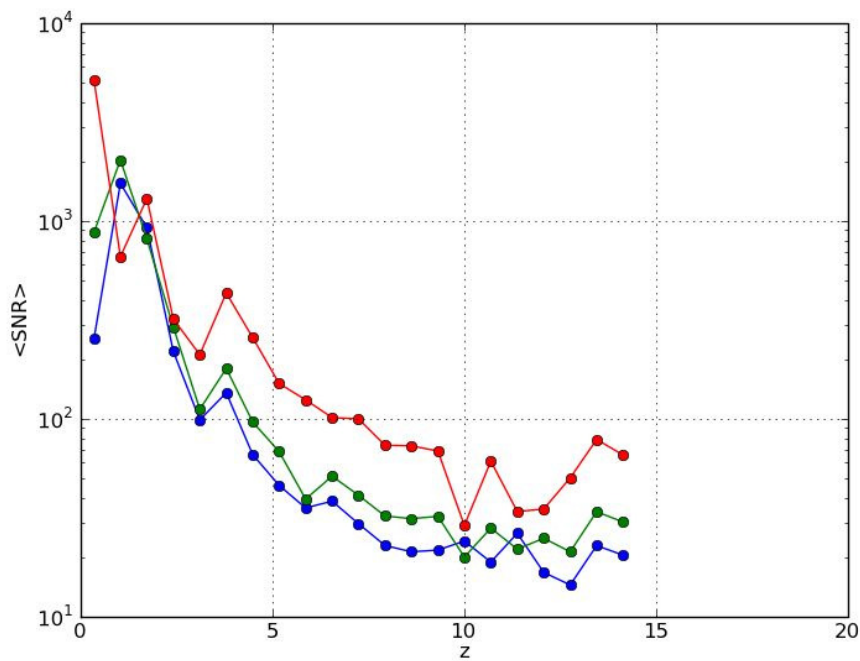


Figure 24: Same as figure 23 but for the LE catalogue.

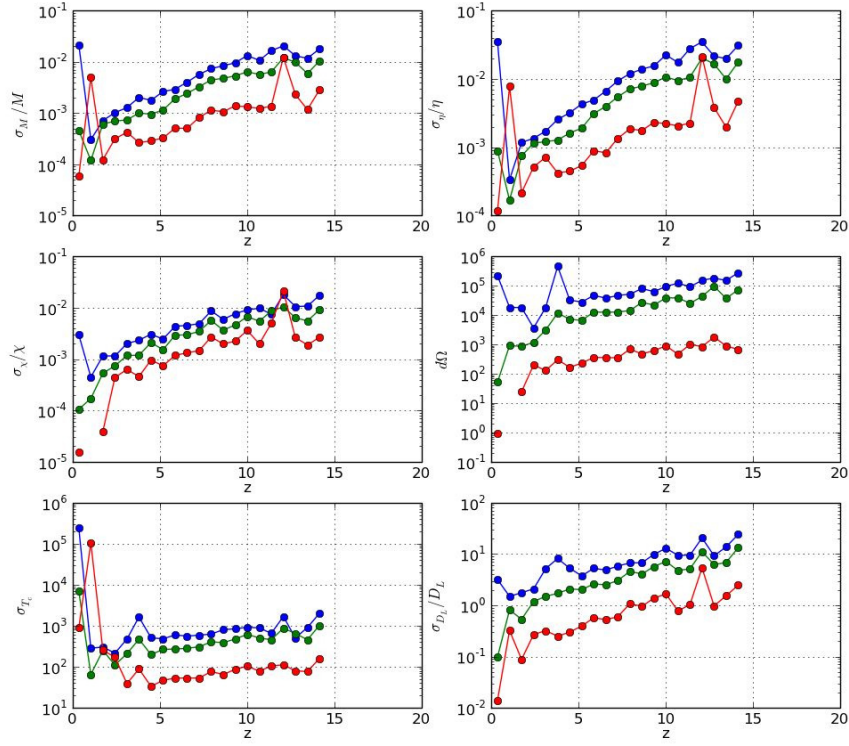


Figure 25: Same as figure 23 but for the LE catalogue.